Smooth Particle Hydrodynamics and Discrete Element Method coupling scheme for the simulation of debris flows ☆

Mario Germán Trujillo-Vela[a,b,c,d], Sergio Andrés Galindo-Torres[a,b], Xue Zhang[d], Alfonso Mariano Ramos-Cañón[c], Jorge Alberto Escobar-Vargas[c]

[a] *Institute of Advanced Technology, Westlake Institute for Advanced Study, 18 Shilongshan St., Hangzhou 310024, Zhejiang Province, China.*
[b] *School of Engineering, Westlake University, 18 Shilongshan St., Hangzhou, Zhejiang 310024, China.*
[c] *Faculty of Engineering, Pontificia Universidad Javeriana, Bogotá, Colombia.*
[d] *Department of Civil Engineering and Industrial Design, University Of Liverpool, Liverpool, United Kingdom.*

Abstract

Debris flows have been widely researched during the last decades since they are catastrophic events with significant infrastructure and environmental impacts. Typically, they are composed of various materials which interactions are worth for studying, to improve the prediction of some variables, such as velocities, forces and affected areas. Constitutive models and numerical methods are fundamental in broadening the knowledge of the behaviour of these phenomena. Thus, the coupling of numerical techniques, for the different constituents of debris flow is becoming indispensable to describe the behaviour of these natural events. The coupling of Smooth Particle Hydrodynamics (SPH) and Discrete Element Method (DEM) is presented in this paper to show the capacity to represent the interaction of several materials at the same time. SPH is employed to represent the fluid and soil by using different constitutive models from a continuum approach. In contrast, DEM is used to represent immersed objects such as boulders and boundary conditions. In this sense, we can couple the behaviour that occurs at very different scales in a unified framework suitable

☆ The code is open source and is available on Mechsys.

*Corresponding author
Email address: s.torres@westlake.edu.cn (Sergio Andrés Galindo-Torres)

to describe heterogeneous debris flows. Benchmark cases were solved to validate this new approach. The simulations show good agreement with analytical solutions, experimental results and field data.

Keywords: SPH-DEM coupling, benchmark validation cases, debris flows

1. Introduction

It is essential to study the movement of mass which occur on earth surface not only to understand the behaviour of nature but also because they can cause great damage and fatalities [1, 2, 3]. There are many types of mass movements such as landslides, debris flows, mudflows, granular flows, rock falls, avalanches, among others. Usually, they are classified depending on certain characteristics such as kind of materials, velocity and volume [4, 5, 6, 7, 8]. The materials can be fluids (water and air) and solids (soil and wood, for instance). The soil has a wide spectrum because of the mineral composition and size of the particles. Thus, clay or sand, and fine grains or big boulders might change the behaviour of the mass [9, p. 3] completely, affecting the procedure to model such phenomena.

Debris flows have special attention in research due to their high potential of damage, provoked by the variability of materials, high velocities and volumes, which might travel long distances destroying everything on their path [10]. Three branches have appeared in an attempt to improve the models. First, some authors have proposed models to represent the movement of a mass from a continuum approach, assuming shallowness for granular flows such as [11, 12, 13, 14]. Others have proposed mixture models where just a single momentum equation contain the stresses terms for two phases (fluid and soil) such as [15, 16, 17]. Finally, [18, 19, 20] have proposed two phases models where a coupling term must be defined. The models mentioned above are postulated in a two-dimensional Eulerian approach.

The improvement of the computational resources and numerical methods has allowed increasing the complexity of modelling these phenomena, adding the third dimension or the interaction with obstacles [21], for instance. Because

of these reasons, the Lagrangian and meshless approaches have been gaining importance. Also, these techniques allow handling complex geometries, interaction with several methods and materials in a more natural way. For example, Smooth Particle Hydrodynamics, SPH henceforth, has been employed to model many cases in soil mechanics and fluid mechanics [22, 23, 24, 25, 26, 27, 28].

SPH has been coupled with other techniques such as Discrete Element Method, DEM henceforth, to represent the interaction with solids [29, 30, 31, 32]. These two methods were developed to tackle problems at different scales: SPH to represent large scales directly by using constitutive laws, and DEM to obtain the general behaviour through the implementation of interaction laws in a small scale of granular assemblies [33, 34]. Nevertheless, DEM can be used to represent big objects with complex shapes as well, been useful to set up boundary conditions, fluid–structures, fluid–soils and fluid–soil–structures interaction problems.

For instance, [29] included rigid bodies into a fluid flow where the discretisation of the solids with SPH particles is still needed. [30] have coupled DEM to the traditional equations that describe the flow in porous media, where the mass conservation equation and the Darcy law are combined, neglecting the momentum equation. An analytical expression gives the interaction force after integrating the pressure on the surface of the spheres. Such pressure is computed by interpolating the variable from the established grid [30]. [31] implemented an algorithm to represent polyhedral DEM particles coupled with fluid SPH particles, where the normal force is based on the pressure of the fluid. [32] modelled rigid and deformable structures that interact with soil SPH particles, which normal force is based on a penetration method.

Also, [35] and [36] represented the soil employing DEM particles and the water using SPH particles, to reproduce landslide induced waves, where the SPH-DEM coupling is based on a drag force term, which involves an empirical formula. Other methods such as Finite Volumes Method (FVM), Finite Elements Method (FEM), Material Point Method (MPM) and Lattice Boltzmann Method (LBM) have been coupled to DEM to predict the interaction of debris

flows with moving and flexible barriers [37, 38, 39]. To model large–deformation problems using mesh-based methods (i.e., FVM, FEM and LBM) requires re-meshing, also meshing areas where there is no flow in a specific time–step. Furthermore, LBM is more convenient for problems where there is not a free surface flow. MPM has demonstrated great advantage in computational cost; however, oscillation in stress calculation is its main disadvantage up to now [40].

It is the purpose of the present work to employ methods that allows us to include several materials and compute large strain in free-surface problems. Hence, this paper presents a new approach to couple SPH-DEM to model natural processes such as debris flows that might be represented by using two standpoints. On the one hand, SPH is used to describe the fluid and soil phases through the continuum assumption. In contrast, DEM is employed to model large boulders as single objects at the same time that the boundary conditions with the sphero-polyhedra approach as presented in [41, 34].

The continuous approach is still employed to have good results at the same time that reasonable computational cost. Besides, discrete elements are employed to avoid the use of extra SPH particles in the boundary conditions or in moving objects which interact the fluid or soil phases.

This paper is organised as follows: Section 2 shows the SPH method and the constitutive models to represent the soil and the water. Section 3 presents briefly the discrete element method. Section 4 contains the proposed strategy for coupling SPH and DEM. Section 5 presents both benchmark cases to validate our code. The last part of this work is presented in Section 6, which shows a hypothetical case of debris flow to test all the interaction forces in one single case. Finally, Section 7 has the conclusions regarding the techniques here employed based on the validation examples.

2. SPH method

SPH is a meshless technique employed to discretised equations which varies with space. This method use an interpolant to find the value of a particular

dependant variable at an arbitrary point, $\mathbf{x}_i$, from the surrounding points, $\mathbf{x}_j$ (Figure 1) [42, 43, 44]. The point $\mathbf{x}_i$ can displace carrying all the information of several variables such as density, velocity, pressure, stresses, strains, among others, depending on the set of equations to be solved [23]. The mass and momentum conservation are the governing equations employed to represent the fluid and soil as a continuum as explain below.

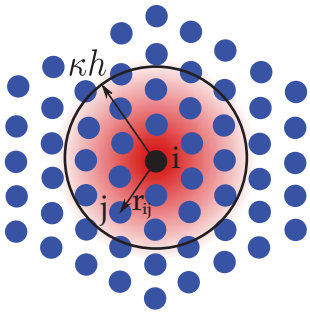

Figure 1: Approximation in SPH method.

2.1. SPH for fluid

The conservation equations to represent the fluid were discretised using the Weakly Compressible (WCSPH) approach, as shown below.

Mass conservation

$$\frac{D\rho_i}{Dt} = \rho_i \sum_{j=1}^{n} \frac{m_j}{\rho_j} \mathbf{u}_{ij} \cdot \nabla_i W(r_{ij}, h) + \delta 2hc_s \sum_{j=1}^{n} \frac{m_j}{\rho_j} (\rho_j - \rho_i) \frac{\mathbf{x}_{ij}}{|\mathbf{x}_{ij}|^2 + 0.1h^2} \cdot \nabla_i W(r_{ij}, h) \tag{1}$$

Momentum equation

$$\frac{D\mathbf{u}_i}{Dt} = \mathbf{g} - \sum_{j=1}^{n} m_j \left(\frac{p_i}{\rho_i^2} + \frac{p_j}{\rho_j^2} + \Pi_{ij} \right) \nabla_i W(r_{ij}, h) + \sum_{j=1}^{n} 4m_j \frac{(\mu_i + \mu_j)}{(\rho_i + \rho_j)^2} \cdot \mathbf{u}_{ij} \nabla_i W(r_{ij}, h) - \mathbf{a}_i^{fs} + \frac{\mathbf{F}_i^{fN}}{m_i} \tag{2}$$

where the subindex i and j denote the point in the matter and the surrounding points, respectively. n is the number of neighbouring particles. $\mathbf{u}_{ij} = \mathbf{u}_i - \mathbf{u}_j$ is the difference of the velocity between the two particles i and j, $\mathbf{x}_{ij} = \mathbf{x}_i - \mathbf{x}_j$ is the vector that contains the distance between the two particles, m is the mass, ρ represents the density, p is the thermodynamic pressure and $\mathbf{g}$ is the gravity. $W(r_{ij}, h)$ the interpolating kernel, ∇_i denotes the gradient of the kernel taken with respect to the coordinates of particle i [45].

The second term in Equation 1 is a diffusive term know as δ-SPH, which is employed to eliminate the noise in the pressure field. There are three versions of δ-SPH, as shown in [46]. However, the version proposed by [47] was implemented to preserve a low computational cost at the same time that a smooth pressure field is obtained. $\delta = 0.15$ is a dimensionless constant. $c_{s(ij)} = (c_{s(i)} + c_{s(j)})/2$ is the average speed of the sound. The $0.01h^2$ term in Equation 1 is included to keep the denominator non-zero. Π_{ij} is the artificial viscosity employed solely when shock wave phenomena are going to be treated, which is presented in detail in [48, 27].

The second and third terms on the right–hand side of Equation 2 were discretised such as proposed by [48] [49] to handle discontinuities. $\mathbf{a}_i^{fs}$ represents the acceleration coming from forces due to the soil particles. $\mathbf{F}_i^{fN} = \mathbf{F}_{i(n)}^{fN} + \mathbf{F}_{i(\tau)}^{fN}$ is the net exerted force on the fluid particle by DEM objects, which is explained below Equation 19. The pressure is computed explicitly by the equation of state proposed by [50]

$$p_i = c_s^2 \left(\rho_i - \rho_0\right) \tag{3}$$

where c_s is the speed of sound; the subscript 0 denotes the initial state of density.

The smooth kernel implemented in this work is the cubic spline [51], defined

as

$$W(r_{ij},h)=\begin{cases}\alpha_d\left(1-\frac{3}{2}q^2+\frac{3}{4}q^3\right), & 0\le q\le 1\\ \alpha_d\frac{1}{4}(2-q)^3, & 1\le q\le 2\\ 0, & q>2\end{cases} \tag{4}$$

where α_d is $7/(478\pi h^2)$ and $1/(120\pi h^3)$ for two and three dimensions, for the unity requirement; $q=r_{ij}/h=|\mathbf{x}_i-\mathbf{x}_j|/h$, is the relative distance between two points and h is the smoothing length. The compact support domain (or influence radius) of this kernel is 2.

2.2. SPH for soil

The mass conservation of soil is the same as Equation 1 without dissipative term, whereas the conservation of momentum is described, such as:

Momentum equation

$$\frac{D\mathbf{u}_i}{Dt}=\mathbf{g}-\sum_{j=1}^{n}m_j\left(\frac{\sigma_i^{'\alpha\beta}}{\rho_i^2}+\frac{\sigma_j^{'\alpha\beta}}{\rho_j^2}+R_{ij}^{\alpha\beta}f_{ij}^n+\Pi_{ij}\delta^{\alpha\beta}\right)\nabla_i W(r_{ij},h) + \mathbf{a}_i^{sf}+\frac{\mathbf{F}_i^{sN}}{m_i} \tag{5}$$

where $\sigma_i^{'\alpha\beta}$ is the effective stress tensor, $R_{ij}^{\alpha\beta}$ is the artificial stress that is added to the components of the stress tensor which were in tension and f_{ij}^n is a suitable function which increases as the separation decreases [52, 27]. Π_{ij} is an artificial viscosity and $\delta^{\alpha\beta}$ is the Kronecker delta.

$\mathbf{a}_i^{sf}$ represents the acceleration coming from forces due to the fluid particles. $\mathbf{F}_i^{sN}=\mathbf{F}_{i(n)}^{sN}+\mathbf{F}_{i(\tau)}^{sN}$ is the net exerted force on the soil particle by DEM objects as shown by Equation 25. If the interaction does not involves a DEM object $\mathbf{F}_i^{Ns}=0$.

The constitutive model that describes the stresses produced by the interaction of soil particles is an elastic-perfectly plastic model in addition to a failure criterion of Drucker–Prager implemented as described in [23, 28]. The constitutive equation can be written as follows,

$$\frac{d\sigma^{\alpha\beta}}{dt} = \dot{\omega}^{\alpha\gamma}\sigma^{\beta\gamma} + \sigma^{\gamma\beta}\dot{\omega}^{\alpha\gamma} + 2G\dot{e}^{\alpha\beta} + K\dot{\varepsilon}^{\gamma\gamma}\delta^{\alpha\beta} - \dot{\lambda}\left[9K\sin\psi\delta^{\alpha\beta} + \frac{G}{\sqrt{J_2}}s^{\alpha\beta}\right] \tag{6}$$

where $\dot{\omega}^{\alpha\gamma}$, $\dot{\varepsilon}^{\gamma\gamma}$ and $\dot{e}^{\alpha\beta}$ are the rotation rate, volumetric and deviatoric strain rate tensors, respectively. $\delta^{\alpha\beta}$ is Kronecker's delta, $\delta^{\alpha\beta} = 1$ if $\alpha = \beta$ and $\delta^{\alpha\beta} = 0$ if $\alpha \neq \beta$. K, G and ψ denote the bulk modulus, shear modulus and the dilatancy angle, respectively. $\dot{\lambda}$ is the rate of the plastic multiplier, λ, which depend on the state of stress and load history, and is defined as following,

$$\dot{\lambda} = \frac{3K\alpha_c\dot{\varepsilon}^{\gamma\gamma} + \frac{G}{\sqrt{J_2}}\dot{\varepsilon}^{\alpha\beta}s^{\alpha\beta}}{27\alpha_c K\sin\psi + G} \tag{7}$$

where $\dot{\varepsilon}^{\alpha\beta}$ and $s^{\alpha\beta}$ denotes the total strain rate and the deviatoric stress tensor. J_2 and α_c are the second invariant of the deviatoric stress tensor and a parameter from Drucker–Prager criterion. For further details, see [23, 28].

2.3. Fluid-soil SPH particle interaction

Equations 8 and 9 are the expressions employed to compute the interaction forces between the two SPH phases, fluid and soil. The interaction forces for the fluid and soil, respectively, are [53, 54, 27, 28]:

$$\mathbf{a}_i^{fs} = \sum_{j=1}^{n} m_s \frac{f^{seepage}}{\rho_f\rho_s} W(r_{fs}, h) \tag{8}$$

$$\mathbf{a}_i^{sf} = \sum_{j=1}^{n} m_f \frac{f^{seepage}}{\rho_f\rho_s} W(r_{fs}, h) - \sum_{j=1}^{n} m_f \frac{p_f}{\rho_f\rho_s}\nabla_i W(r_{sf}, h) \tag{9}$$

The subindex f and s denote fluid and soil particle, respectively. The second term in Equation 9 represents the pore fluid pressure exerted on soil particles. $f^{seepage}$ is the seepage force based on Darcy's law, which is defined as follows

$$f^{seepage} = \frac{\mu}{k}(\mathbf{u}_f - \mathbf{u}_s) \tag{10}$$

where $k = k_h \mu / \rho_f g$ is the intrinsic permeability, k_h is the Darcy hydraulic conductivity (unit, L/T), μ and ρ_f are the fluid viscosity and density, respectively. Dimensionally, k is an area (L^2) [55, p. 89]. By using a laboratory-scale series of experiments, [27, 28, 56, 57] have demonstrated that the physics implemented in this work for the coupling of soil-water interaction forces can produce satisfying agreements with experimental data. Because of this validations, the authors will focus on the validation with DEM in this paper.

3. DEM

DEM was proposed to represent granular assemblies that are treated as distinct objects by definition [33], where an interaction law among the particles is defined. Sphero-polyhedra approach of DEM is implemented in this work, which characteristic is given by a sphere radius, henceforth DEM halo, defined in Section 4 and widely described in [58]. The momentum equation of the DEM objects is given by the second Newton's law, thus;

$$m_k \frac{D\mathbf{u}_k}{Dt} = m_k \mathbf{g} + \sum_{i=1}^{n} \mathbf{F}_i^{Np} \tag{11}$$

where m is the mass, $\mathbf{u}$ is the velocity, $\mathbf{g}$ the gravity and $\mathbf{F}_i^{Np} = \mathbf{F}_{i(n)}^{Np} + \mathbf{F}_{i(\tau)}^{Np}$ is the exerted force on the DEM element by a SPH particle i of any SPH phase p (fluid or soil). Respectively, $\mathbf{F}_{i(n)}^{Np}$ and $\mathbf{F}_{i(\tau)}^{Np}$ are the normal and tangential force that are defined in Section 4.

4. Coupled SPH-DEM

As mentioned above, any DEM particle (sphere, segment (2D) and plane) is treated with the Sphero-polyhedra approach. One single DEM particle will represent the DEM object, and there are not other SPH particles to represent or discretise the DEM objects. All DEM particles have a halo to avoid any "penetration" between SPH and DEM. Before starting any computation between the two methods, it is necessary to verify if the DEM object is inside the

range radius (i.e., the compact support domain κh) of the SPH particle in the matter. The main idea of this interaction approach is that the algorithm seeks the closest contact point between a DEM particle (sphere, segment or plane) and the SPH particle in concern. When the DEM particle is a segment, as the SPH particle (blue particle) is located, the virtual SPH particle (purple particle) will be placed based on the minimum distance (Figure 2b). This part of the algorithm is explained in detail in [41]. If the object is a sphere, a virtual SPH particle will be placed at the nearest point on the surface of the sphere (Figure 2a). Such virtual SPH particle will be placed as long as SPH particle is close enough to the DEM particle. Then, a point on the surface of the DEM sphere $\mathbf{x}_s$ is found by using the following expression,

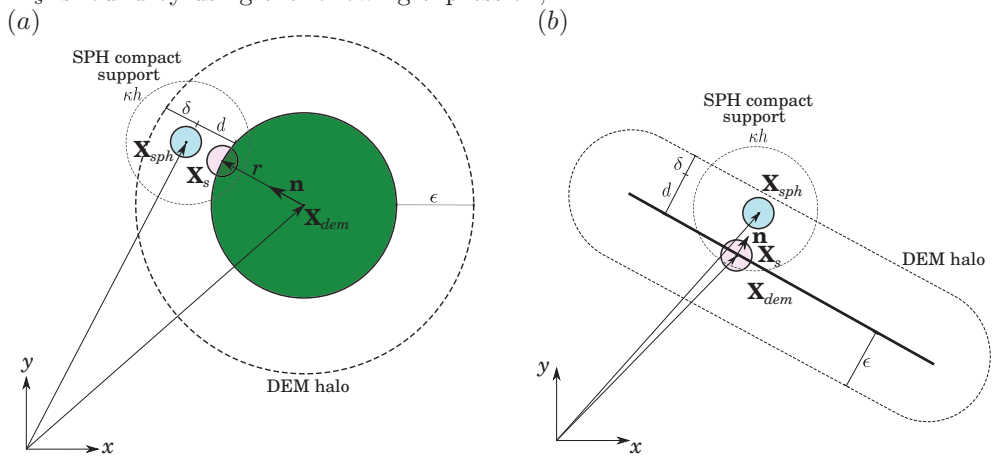

Figure 2: Coupling SPH-DEM scheme. (a) DEM sphere interacting with SPH particles. (b) DEM segments or planes are interacting with SPH particles. The blue particle represents the SPH particle, the purple particle is a virtual particle, and the circular and flat objects are DEM particles, whose positions are $\mathbf{x}_{sph}$, $\mathbf{x}_s$, and $\mathbf{x}_{dem}$, respectively.

$$\mathbf{x}_s = \mathbf{x}_{dem} + r\mathbf{n} \tag{12}$$

Thus, $\mathbf{x}_s$ gives the position of the virtual SPH particle (purple particle in Figure 2) to compute the interaction between SPH real particle (blue particle in Figure 2) and the surface of the DEM particle. r is the radius of the sphere and $\mathbf{n} = (\mathbf{x}_{sph} - \mathbf{x}_{dem})/|\mathbf{x}_{sph} - \mathbf{x}_{dem}|$ is the unit normal vector, $\mathbf{x}_{sph}$ is the

position of the SPH particle and $\mathbf{x}_{dem}$ is the centre of the DEM object. Then, the distance between the real and virtual particle is given by

$$d = |\mathbf{x}_{sph} - \mathbf{x}_s| \tag{13}$$

Finally, the overlapping distance δ between the SPH particle and the DEM halo is computed as follows (Figure 2),

$$\delta = \epsilon - d \tag{14}$$

where ϵ is the thickness of the halo. In this study, it has been verified that a value of the half of the initial SPH particle distribution (i.e., $\epsilon = \Delta x/2$) seems to be appropriate.

When the distance between the SPH particle and the DEM object surface is lower than the compact support domain (i.e., $d < \kappa h$). then, the tangential force for fluid-DEM interaction will be computed as shown in Section 4.1. On the other hand, if the overlapping distance between the SPH particle and the DEM halo is greater than zero (i.e., $\delta > 0$), then the tangential force for the soil-DEM interaction can be computed as shown in Section 4.2.

In contrast, the normal force is computed indistinctly of the involved phase (soil or water) by assuming an elastic interaction defined as

$$\mathbf{F}_{i(n)}^{Np} = K_n \delta \mathbf{n} \tag{15}$$

where K_n and $\mathbf{n}$ are the normal stiffness coefficient and the normal unit vector. The value of the normal stiffness is computed as $K_n = 0.1 m_{min}/\Delta t^2$, being m_{min} the minimum value of the mass over all the particles inside the domain either SPH or DEM particles, and Δt is the computational time–step. The equation employed to compute the normal stiffness is based on the oscillation period of a single degree of freedom, as explained in [59]. The time–step is selected as the minimum required to keep the stability of SPH particles, either fluid or soil. Besides, an adaptative time–step is employed as detailed presented by [28]. The normal force is dependent on the allowed penetration of the SPH

particle into the DEM halo. Thus, pressure or normal stresses are not employed in such purpose. The total force exerted on DEM objects is the summation of the force coming from all SPH particles that interact with it, as shown in Equation 11. This definition of the normal force ensures that the SPH particle does not break through the DEM particles and the normal stiffness expression guarantees the stability of the solution [60, 32, 61]. Now, let us define the relative velocity between the SPH particle and DEM object such as,

$$\mathbf{u}_{rel} = \mathbf{u}_{sph} - \mathbf{u}_{dem} - \boldsymbol{\omega}_{dem} \times (\mathbf{x}_s - \mathbf{x}_{dem}) \tag{16}$$

where $\boldsymbol{\omega}_{dem}$ is the angular velocity of the DEM object, $\mathbf{x}_{dem}$ is the position of the centre of the DEM particle and $\mathbf{x}_s$ is point on the surface of the DEM object (virtual SPH particle) (Figure 2). After the previous calculations, the following steps depend on what SPH material (fluid or soil) is interacting with the DEM object as it will be explained below.

4.1. Fluid-solid interaction force

The interaction term between the SPH fluid particle and DEM is defined by an extra viscous term $\mathbf{a}_\tau$ (Equation 17) with the same form as appear in Equation 2.

$$\mathbf{a}_\tau = \frac{1}{\rho_i} \nabla \cdot (\mu_i \nabla \mathbf{u}_i) = \frac{4 m_i}{3 h^D} \frac{(2\mu_i)}{(2\rho_i)^2} \frac{\mathbf{u}_{rel}}{d} \frac{\nabla_i W(d,h)}{W(0,h)} \tag{17}$$

The expression $2\rho_i$ is because the density of the virtual particle equals the density of the real SPH particle i, and the same principle is employed with the viscosity μ_i. d is the distance between the real and virtual SPH particle. The additional term that multiplies Equation 17 might be written separately as

$$\frac{2}{3h^D} \frac{1}{W(0,h)} \tag{18}$$

where D is the dimensionality of the problem. Since one single virtual SPH particle is "created" to compute the viscous interaction between SPH and DEM

particles, deficiencies in the calculation of the viscous force might appear. Hence, Equation 18 is employed to compensate such deficiency, which corresponds to the readjusted normalising constant in a similar way as suggested by [31].

Then, the total force exerted from the DEM object to the SPH particle is described as follows;

$$\mathbf{F}_i^{fN} = \mathbf{F}_{i(n)}^{fN} + m_i \mathbf{a}_\tau \tag{19}$$

where the normal force $\mathbf{F}_{i(n)}^{fN}$ is computed as shown in Equation 15 and the second term on the right hand is the tangential force for fluid-DEM interaction $\mathbf{F}_{i(\tau)}^{fN} = m_i \mathbf{a}_\tau$. Equation 19 shows the net force exerted on the SPH particle by a DEM element.

Since the third Newton's law governs the interaction force, Equation 20 shows the net force exerted on the surface of a DEM object.

$$\mathbf{F}_i^{Nf} = -\mathbf{F}_{i(n)}^{fN} - m_i \mathbf{a}_\tau \tag{20}$$

By using the net force, it is possible to obtain torque exerted on the surface of the DEM particle as follows.

$$\mathbf{T} = \mathbf{F}_i^{Nf} \times (\mathbf{x}_s - \mathbf{x}_{dem}) \tag{21}$$

Once all the torques are calculated, the Euler equations for the angular momentum is integrated using the Leap-Frog algorithm as described in [62, 63].

4.2. Soil-solid interaction force

When the soil particle is interacting with a DEM object, the normal force $\mathbf{F}_{i(n)}^{sN}$ will be computed in the same when the interaction is fluid-DEM, Equation 15. Whereas the frictional force depends on the relative velocity and the friction coefficient. Thus, the tangential velocity is defined as follows [32],

$$\mathbf{u}_\tau = \mathbf{u}_{rel} - (\mathbf{u}_{rel} \cdot \mathbf{n})\mathbf{n} \tag{22}$$

The tangential component of the contact force acting on soil particle i can be computed using the following steps,

$$\boldsymbol{\delta}_\tau = \boldsymbol{\delta}_\tau + \Delta t \mathbf{u}_\tau \tag{23}$$

where Δt is the time–step and $\boldsymbol{\delta}_\tau$ the distance on which the SPH particle and the DEM particle are suffering tangential contact. The rectification of the tangential distance is given as shown by Equation 24.

$$\boldsymbol{\delta}^*_\tau = \begin{cases} \frac{\mu_\phi |\mathbf{F}_n|}{K_n} \mathbf{n}_\tau, & \text{if } |\boldsymbol{\delta}_\tau| > \mu_\phi |\mathbf{F}_n| / K_n \\ \boldsymbol{\delta}_\tau, & \text{otherwise} \end{cases} \tag{24}$$

where μ_ϕ is the frictional coefficient between soil and the surface of the structure, and $\mathbf{n}_\tau = \boldsymbol{\delta}_\tau / |\boldsymbol{\delta}_\tau|$ when $|\boldsymbol{\delta}_\tau| > 0$ to avoid division by zero. The net force acting on the soil particle i is given by Equation 25.

$$\mathbf{F}^{sN}_i = \mathbf{F}^{sN}_{i(n)} - K_n \boldsymbol{\delta}^*_\tau \tag{25}$$

The normal force $\mathbf{F}^{sN}_{i(n)}$ is computed as shown in Equation 15 and the second term on the right hand is the tangential force for soil-DEM interaction $\mathbf{F}^{sN}_{i(\tau)} = K_n \boldsymbol{\delta}^*_\tau$. The net force exerted on the DEM object satisfies the third Newton's law. Thus,

$$\mathbf{F}^{Ns}_i = -\mathbf{F}^{sN}_{i(n)} + K_n \boldsymbol{\delta}^*_\tau \tag{26}$$

Also, the torque is computed by using the net force as below,

$$\mathbf{T} = \mathbf{F}^{Ns}_i \times (\mathbf{x}_s - \mathbf{x}_{dem}) \tag{27}$$

Once all the torques are calculated, the Euler equations for the angular momentum is integrated using the Leap-Frog algorithm as described in [62, 63].

SPH is well known to suffer over volumetric deformation in any phase, fluids and solids, even in hydro or geostatic conditions [46]. In the present work, such

an issue was also found through the free surface cases. However, such deformation seems not to affect the SPH-DEM coupling directly since the interaction forces are defined in term of the mass, which is exactly preserved unlike density and consequently the volume. This can be noticed especially in soil mechanics modelling interacting with the DEM particles (Equations 25 and 26).

5. Validation cases

5.1. Poiseuille flow

A simple case of Poiseuille flow was carried out to validate the proposed approach. A key component of the SPH-DEM coupling is the force exerted on DEM particles by SPH given by Equations 20 and 26. These equations are used to calculate the force exerted on DEM particles and compare them with the analytical solutions. For this case, the fixed boundaries of Poiseuille flow are represented by flat DEM particles. The Poiseuille flow is given between two stationary parallel infinite plates (herein simulated by DEM fixed particles) at $y = 0$ and $y = H$ (Figure 3). A constant acceleration a drives the fluid when $t > 0$ s under a laminar regime. The main assumptions to describe this process is that the fluid is Newtonian, and the boundary conditions are non-slip. The series solution for the transient behaviour is by the Equation 28 [48].

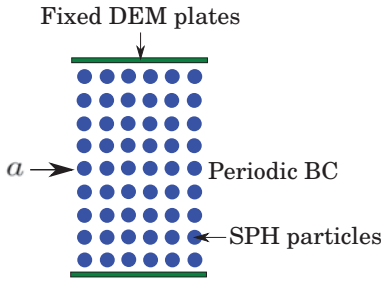

Figure 3: Sketch of SPH-DEM coupling for Poiseuille problem.

$$u(y,t) = \frac{a}{2\nu} y(H-y) - \sum_{n=0}^{\infty} \frac{4aH^2}{\nu\pi^3(2n+1)^3} \sin\left(\frac{\pi y}{H}(2n+1)\right) \cdot \exp\left(-t\frac{(2n+1)^2\pi^2\nu}{H^2}\right) \quad (28)$$

where u is the velocity in x direction, $\nu = \rho/\mu$ is the kinematic viscosity, ρ is the density and μ the viscosity. When $t \to \infty$, the flow reach the stationary condition that is described by Equation 29.

$$u(y, t \to \infty) = \frac{a}{2\nu} y(H-y) \quad (29)$$

On the other hand, the force over a layer of fluid or the boundaries can be described by the Newton viscosity law as shown by Equation 30.

$$F_x(y, t \to \infty) = \tau A = \mu \frac{\partial u}{\partial y}(l \times 1) \quad (30)$$

where τ is the main the shear stress, and $A = l \times 1$ is the area of the applied force, been l the length in x direction by unity in the z direction. By replacing Equation 28 into Equation 30 and after derivation, it is possible to obtain

$$F_x(y,t) = \rho a \left(\frac{H}{2} - y\right) l - \sum_{n=0}^{\infty} \frac{4\rho a H^2}{\pi^3(2n+1)^3} \left(\frac{\pi}{H}(2n+1)\right) \cos\left(\frac{\pi y}{H}(2n+1)\right) \cdot \exp\left(-t\frac{(2n+1)^2\pi^2\nu}{H^2}\right) l \quad (31)$$

Equation 31 describes the force as a function of height and time. The force at the stationary state is described by Equation 32

$$F_x(y, t \to \infty) = \rho a \left(\frac{H}{2} - y\right) l \quad (32)$$

The case is solved by using the following parameters as $a = 10^{-4}$ m/s^2, $y = [0, H]$ m, $H = 10^{-1}$ m, $l = 10^{-1}$ m, $\rho = 1000$ kg/m^3, $\mu = 10^{-1}$ Pa-s,

$\nu = 10^{-4}$ m^2/s, $t = [0, t \to \infty]$ s. The Reynolds number is $Re = 1.3$, which belongs to the laminar regime. No dissipation terms were needed in this case. Figure 4 compares the analytical solution to the numerical solution given by two methods in the boundary, SPH and DEM. The coupled SPH-DEM produce results as good as the pure SPH method.

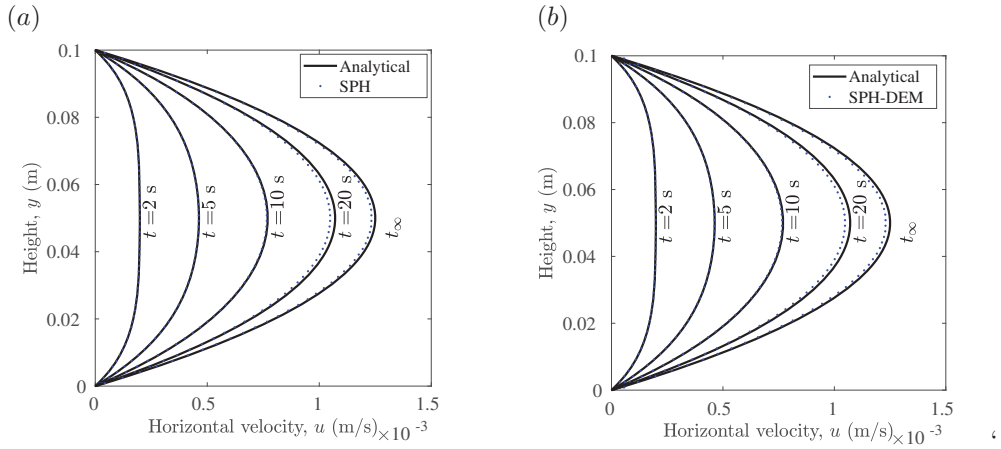

Figure 4: Vertical velocity profile comparison to the analytical solution (Equation 28). (a) SPH velocity obtained by the use of SPH boundary particles and (b) SPH velocity obtained by the use of DEM plates at the boundaries.

Figure 5 compare the force obtained by the Equation 31 to the force obtained numerically on the DEM plates computed as shown in Equation 20. Figure 6 shows the Euclidean norm (Equation 33) of the error as a function of the time produced in the velocity profile when using SPH or DEM boundary conditions. It is possible to see that there is no difference between the two treatments. Also, Figure 7 shows the Euclidean norm of the error generated by the computation of the force on the DEM plates solely as a function of time. Although the oscillations are noticeable, the order of magnitude for this specific example is very low O(10^{-6}).

$$||e||_2 = \sqrt{\sum_{i=1}^{n} (u_a - u_n)_i^2} \tag{33}$$

where u_a and u_n are the velocity in x direction obtained by the analytical and numerical solution, respectively.

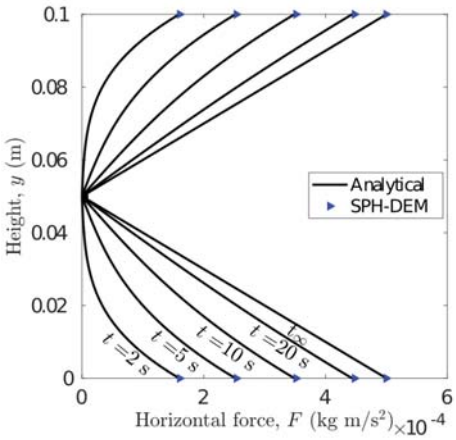

Figure 5: Comparison of the force profile (solid line) given by the analytical solution (Equation 31) to the numerical solution given by Equation 20 (blue triangles).

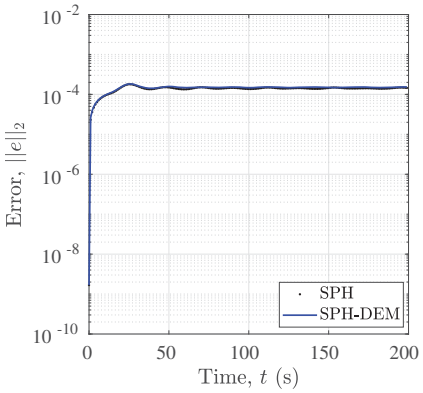

Figure 6: Euclidean norm of the error of the velocity profile as a function of time for both treatments at the boundary conditions, SPH dummy particles and DEM plates.

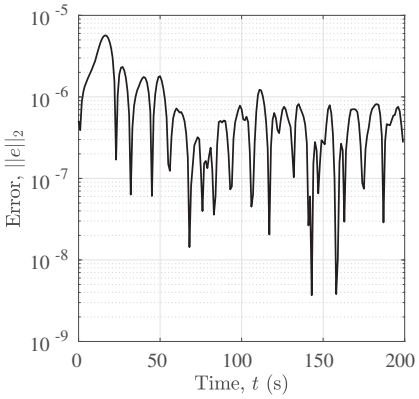

Figure 7: Euclidean norm of the error of the force obtained on the DEM plates as a function of the time.

5.2. Square array of cylinders immersed in fluid

The goal now is to test the coupling law for SPH fluid particles with curved DEM surfaces. Hence, a flow given through an array of cylinders is implemented, which is typically employed to represent flow in porous media. The flow is assumed to be in a steady motion driven by an acceleration a, and the fluid is incompressible (Figure 8). The dimensionless force exerted on a periodic square array of cylinders per unit length is given as [64, p. 167],

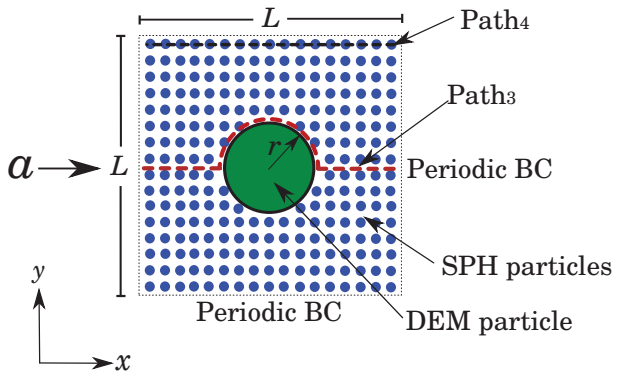

Figure 8: Square array of cylinders (DEM particle) immersed in a fluid flow (SPH particles). Paths for comparison 3 and 4.

$$\frac{F}{\mu \bar{U}} = \frac{4\pi}{k^*(c)} \tag{34}$$

where $\bar{U}$ is the seepage velocity in x direction, and $k^*(c)$ is the dimensionless permeability which is a function of the solid concentration defined as $c = \pi r^2/L^2$. The force F is computed by using the coupling Equations 19 and 20. The total force exerted on the unique DEM particle is obtained by the summation of the force coming from all the SPH particles that interact with the DEM surface (Equation 11). The simulation was performed for several solid concentration, which means that the length L was kept as constant, whereas, the radius r was changed as can be observed in Figure 11.

The solution is given in two dimensions by discretising the fluid with SPH whereas the cylinder is represented by a DEM sphere as shown in Figure 8. The

boundary conditions are imposed as periodic. The paths 3 and 4 highlighted in Figure 8 are employed to compare the solution here obtained to the results given employing FEM in [48] (Figure 10). The case is solved under the following conditions. The flow is driven by a body force $a = 2 \times 10^{-5}$ m/s^2 in x direction. $x = y = [0, L]$, $L = 2 \times 10^{-1}$ m, $\rho = 1000$ kg/m^3, $\mu = 10^{-1}$ Pa-s, $\nu = 10^{-4}$ m^2/s, $t = [0, t \to \infty]$ s, and the number of nodes was 100×100. Taking the scale of the DEM particle inside the fluid, the Reynolds number is between $Re \approx 0.0023$ for a high solid concentration, and $Re \approx 0.1224$ for the low solid concentration, which belongs to the laminar regime. The artificial viscosity term was used for this case, where the values for the dissipation parameters were $\alpha = \beta = 0.01$. The stability of this case was ensured by the following equations

$$C_s = \sqrt{\frac{ar\rho}{\Delta\rho}}; \qquad \Delta t = CFL\frac{h}{C_s} \tag{35}$$

where, C_s is the speed of the sound, $\Delta\rho = 3\%$ is the allowed variation in density and $CFL = 0.005$ is the stability condition. This values allows to obtain a smooth field pressure when δ-SPH is used (Figure 9d).

Figure 9 shows the solution of the problem postulated in this section. Figures 9a and 9b present the velocity and pressure field, respectively, with no density dissipation. Figure 9c and 9d give the velocity and pressure field, respectively, employing δ-SPH. It is notorious the improvement of the solution given in the pressure field when δ-SPH is used, whereas there is not significant affection in the velocity field. Also, Figure 10 compares the solution given by our coupled SPH-DEM with δ-SPH to a FEM solution presented in [48]. The parameters and dimensions were changed for this very specific case, as is described in [48]. The coupled methods show suitable results with respect to the FEM solution.

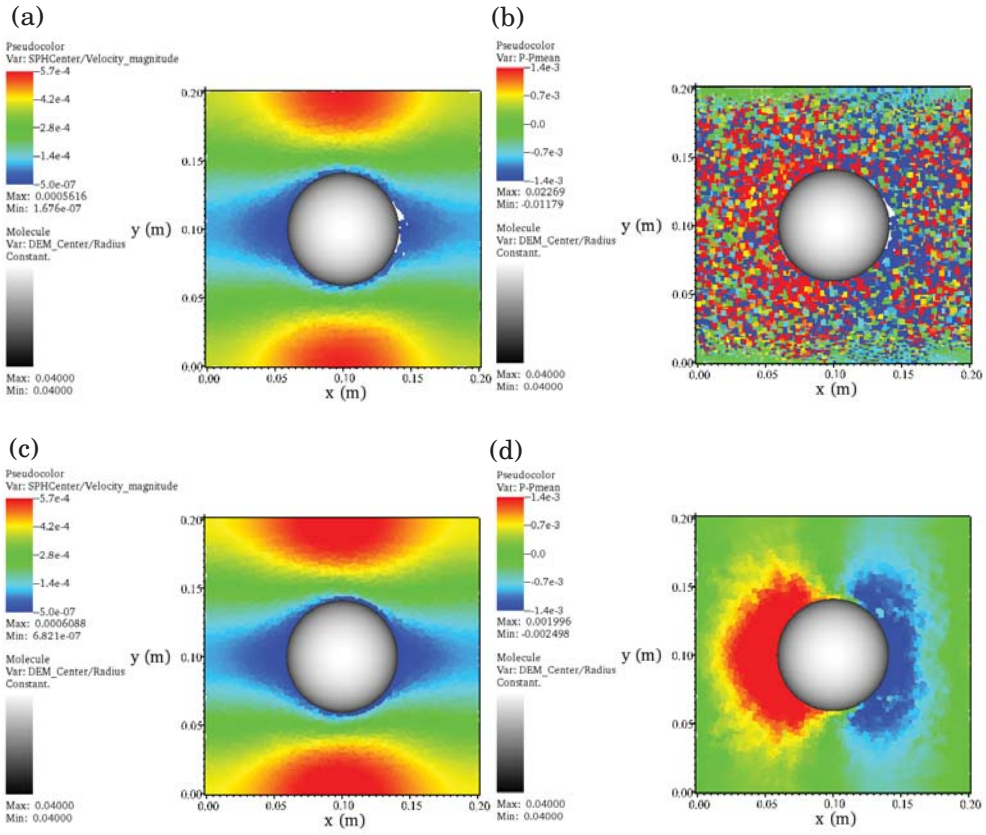

Figure 9: (a) Velocity distribution (u, m/s) and (b) pressure field ($p - p_{mean}$, Pa) of the flow with an immerse DEM sphere when the boundary conditions are set up as periodic and the solid concentration $c = 0.125$.

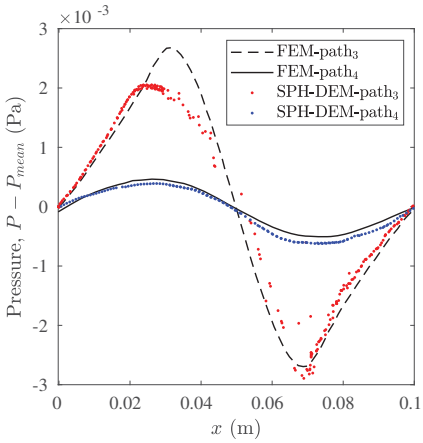

Figure 10: Comparison of pressure produced by the SPH-DEM coupling to the solution given by FEM presented in [48].

Figure 11 compares the dimensionless permeability given by the numerical solution computed using SPH-DEM coupled method to its analytical solution. It is necessary to calculate the coupling force through Equations 19 and 20 to replace it in Equation 34, which allows us to obtain the dimensionless permeability. The analytical values were taken from the tabulation presented in [64, p. 169][65]. Figure 11 shows the permeability computed with and without the dissipation term for the density (i.e., δ-SPH). Although, δ-SPH produce a nearly no noisy pressure field, as shown in Figure 9, the dimensionless permeability present a higher overestimation (Figure 11). In spite of the differences, the results obtained using SPH-DEM are in close agreement with the analytical ones.

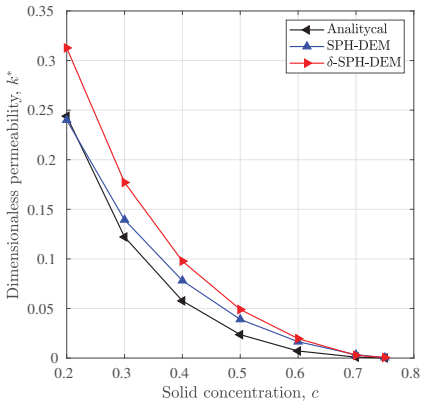

Figure 11: Comparison of the dimensionless permeability to the analytical solution taken from [65, 64].

5.3. Dry granular flow impact on an immovable wall

The tests of the coupled SPH-DEM have shown acceptable results for steady-state water flows. However, it is also important to test the method with discontinuous processes such as sharp wavefronts and its impact on immovable walls. Furthermore, it is also needed to validate the SPH soil particles interacting with DEM objects as it was performed with SPH fluid coupling. Therefore, an experiment of a dry granular flow developed by [66] was attempted to be reproduced using our coupled model. The experiment was generated using 50 kg Toyoura sand with a bulk density of 1379 kg/m^3. The mean grain diameter is about 0.25 mm, and the mean porosity was 0.435 as taken by [67]. The parameters to reproduce the experiment numerically are summarised in Table 1. The sand was contained in a box which gate was suddenly released. The length and width of the flume were 1.8 m and 0.3 m, respectively. An immovable wall was located at a distance of 1.8 m, which was able to measure the impact force. The basal surface of the channel was coated with sand to increase friction. The experiment was developed for different inclination angles 45°, 50°, 55°, 60° and 65° [66].

Table 1: Parameter to reproduce the experiment of the dry granular flow.

Parameter	Units	Value
Bulk density, ρ_s	kg/m^3	1379
Friction angle, ϕ	$^\circ$	26
Dilation angle, ψ	$^\circ$	0
Young modulus, E	MPa	10
Cohesion, c	kPa	0
Poisson ratio, ν		0.3
Porosity, n		0.435
Gravity, g	m/s^2	9.81
Bed friction coefficient, μ_ϕ		$\tan 26^\circ$

The case was simulated in 3D by discretising the space with SPH particles to represent the sand, and DEM planes to set up de boundary conditions. The initial condition has the following dimensions $0.5 \times 0.3 \times 0.3$ m, length, width, and high, respectively, as shown in Figure 12. The spacing among the SPH points was $\Delta x = \Delta y = \Delta z = 0.0125$ m, for a total of 20631 SPH particles. Also, an artificial viscosity term was used for this case, where the values for the dissipation parameters were $\alpha = \beta = 1.0$. A good fitting was found by employing this friction angle as well as the dissipation parameters as indicated by [26, 25] for granular flows.

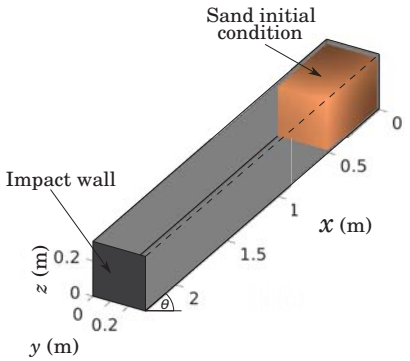

Figure 12: Initial condition of the dry granular material inside the flume. The gray and black planes are DEM objects and the brown box is composed of SPH particles.

Figure 13 shows the longitudinal profile of the mass going down a flume with a slope angle $\theta = 45°$ at six time–steps. The colour map shows the magnitude of the velocity. The front of the descending mass has the highest velocity, about 3.5 m/s, similar to the results obtained by [66] whereas the tail has a low velocity. Also, it is possible to see when the mass starts to be accumulated once it reaches the wall and how the flow over-tops the wall as describe by [66].

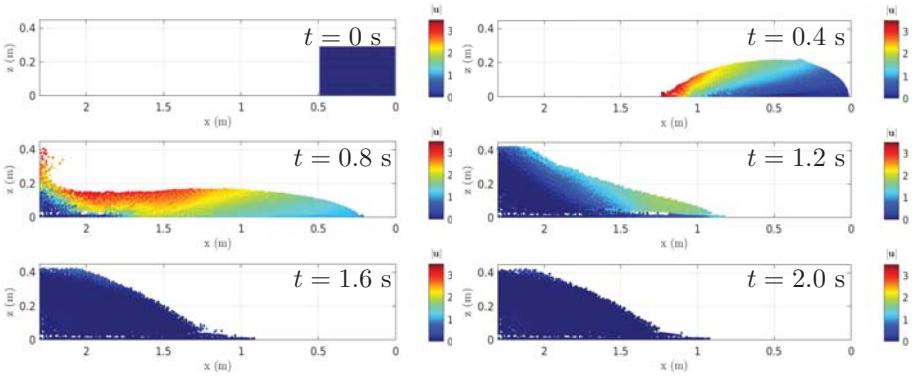

Figure 13: Lateral view of the dry granular flow with a slope angle $\theta = 45°$. The colour map indicates the norm of the velocity vector $|\mathbf{u}|$ of the SPH particles.

Figure 14 compares the measured impact force in the experiment given by

[66] as a function of the time to the 3D numerical simulation generated by the coupled SPH-DEM method when the inclination angle $\theta = 45°$. Thus, it is possible to validate the coupling force presented in Equations 25 and 26 when wave fronts of soil SPH particles impact a rigid wall. The experiment and numerical results match within an acceptable tolerance. The "post-peak" values are nearly the same in both situations despite the "peak force" is overestimated. Also, a slight advance on the arrival of the mass to the wall can be noticed in Figures 13 and 14.

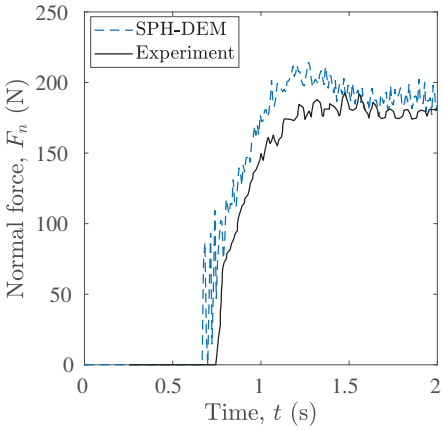

Figure 14: Comparison of the impact force obtained from the experiment of the dry granular flow generated by [66], and the SPH-DEM simulation.

The Figure 15 shows the "peak force" measured in experiments performed by [66], as well as, the numerical solution obtained by the coupled SPH-DEM and [68]. The curves and the "peak force" is consistent with the experimental results for an inclination angle of 45°. However the "peak force" are overestimated in the remainder of the angles.

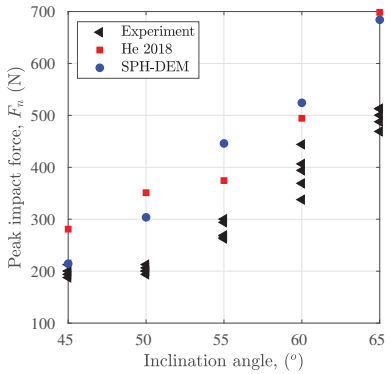

Figure 15: Comparison of the peak impact force obtained from the experiment of the dry granular flow generated by [66], the numerical results from [68], and the solution provided by the coupled SPH-DEM.

This granular flow has been reproduced by several authors to test other approximations. Table 2 shows the main characteristics of the SPH models presented in [21], [68] and the present work to solve the impact force problem. Each solution employed a different constitutive model, whereas none of the other authors has employed DEM boundary conditions. Despite all the differences our model produced closer results to [68] than [21] as can be noticed in Figure 15.

Table 2: The main differences of SPH models employed to solve the impact force problem.

Author	EOS	Constitutive equation	BC
[21]	Weakly-compressible	Bingham model	SPH
[68]	Incompressible	Mohr-Coulomb	SPH
SPH-DEM	Weakly-compressible	Druker-Praguer	DEM

EOS: equation of state, BC: boundary condition.

The small differences in width between the flume and the container given in the experiment set up might be the cause of the impact force overestimation, such as suggested by [68] even when the simulation was performed in 3D. By another hand, the bulk density, friction angles and artificial viscosity parameters significantly contribute to obtaining an appropriate and less noisy impact force

estimation. Despite this, it is the author's opinion that the obtained match validates the proposed coupling scheme.

5.4. Real scale dry landslide

Furthermore, from the author's experience, traditional dummy SPH particles for the boundary conditions ([51, 69]) added to the constitutive model can influence the run-out distance of long-distance travel landslides. Hence, it is crucial to test the coupled method using larger-scale problems such a the Yangbaodi landslide that occurred in Southern China in 2002 [70]. The simulation of the Yangbaodi landslide is presented by [70] in 2D, employing a scheme called Particle Finite Element Method (PFEM). The reproduction 2D case denotes that a plane strain was assumed, which imply that the strain in the third direction can be neglected in comparison with the horizontal and vertical ones. Also, [71] presents a 2D simulation of the same event employing DEM particles solely. The previously mentioned works presented the simulation in dry conditions, unlike the real event that was triggered by accumulated rainfall. Calibration in bed friction angle and friction coefficient were employed in PFEM and DEM, respectively, to compensate the pore fluid pressure lack and obtain the observed run-out distance in the field. The same dry condition with the continuum approach is employed in this validation case in order to test the pure bed frictional SPH-DEM coupling in large-scale problems based on the reference solutions given by [70, 71].

Hence, the simulation was executed by employing SPH particles to represent the dry soil, whereas the boundary conditions are set up as DEM plates 2b. This example allows to validate the coupling force defined in Equations 25 and 26 in natural scale environments, where larger amount of energy and higher velocities are occurring during the mass movement.

Figure 16 shows the initial configuration of the sliding mass, topography and the maximum run-out distance registered from the real case. The thickness of the soil is between 3 and 8 m, and the slope angle about 20° - 25°. The registered length and thickness of the deposit were 140 m and 1-5 m, respectively.

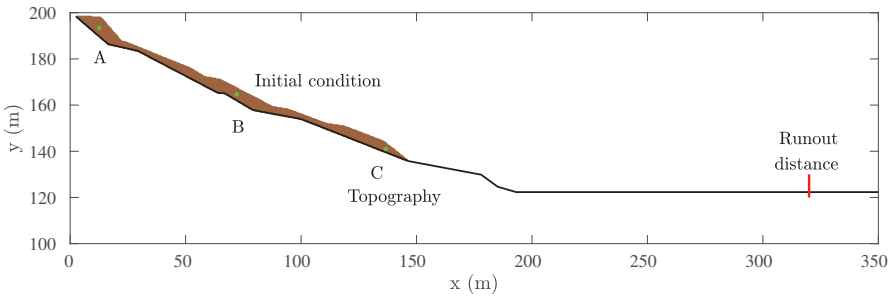

Figure 16: Initial configuration of the Yangbaodi landslide. Three tracked points (green points A, B and C).

The sliding mass was discretised by using a $\Delta x = \Delta y = 0.38$ m with a total of 3496 SPH particles akin to [70]. The boundary conditions were set up as DEM segments with a friction coefficient of $\mu_\phi = \tan 10°$. The final time of the simulation was 30 s. The imposed parameters for the dry simulation of the Yangbaodi landslide were taken from [70, 71] and, are summarised in Table 3. Figure 17 shows the mass descending by the slope at six time–steps. The colour map shows the magnitude of the velocity of each SPH particle.

Table 3: Parameter to reproduce the Yangbaodi landslide in dry conditions. Taken from [70, 71]

Parameter	Units	Value
Soil density, ρ_s	kg/m^3	1133.98
Friction angle, ϕ	°	28
Dilation angle, ψ	°	0
Young modulus, E	MPa	10
Cohesion, c	kPa	0
Poisson ratio, ν		0.3
Porosity, n		0.428
Gravity, g	m/s^2	9.81
Bed friction coefficient, μ_ϕ		$\tan 10°$

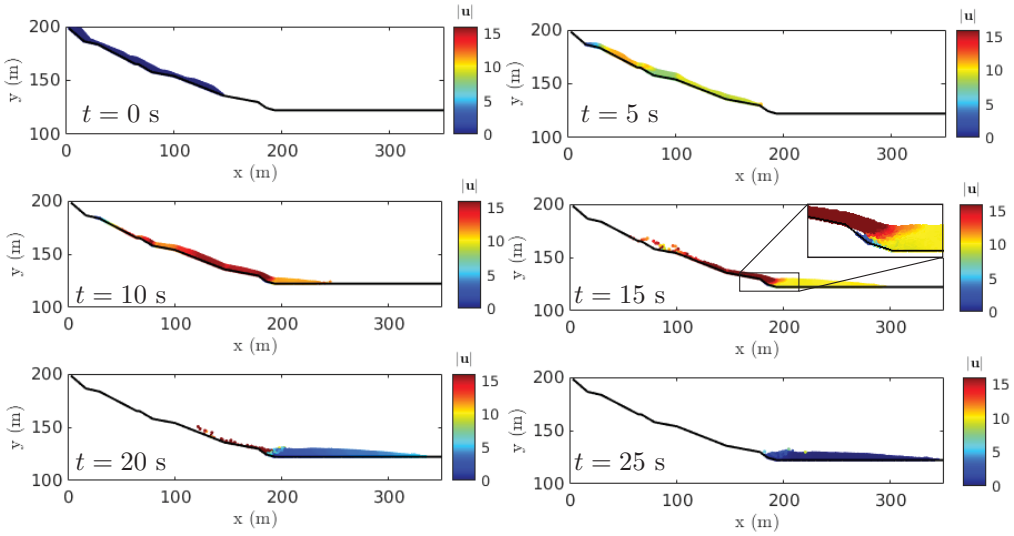

Figure 17: Norm of the velocity vector $|\mathbf{u}|$ of SPH particles going down the slope.

Figure 18a and 18b compare the SPH-DEM coupled method to the solution produced by the Particle Finite Element Method (PFEM) presented in [70]. The comparison of the coupled SPH-DEM is given to the PFEM since both simulations were performed with the continuum approach. Moreover, the solution given by PFEM was already validated with a more standard method, pure DEM, showing similar results [70]. The velocity in x and y direction for each tracker point A, B and C are compared with the two above mentioned numerical methods in Figures 18a and 18b, respectively. The velocity that is given by the PFEM (solid green line) and SPH-DEM (dashed blue line) have similar behaviour, and it is especially remarkable on the abrupt changes. The information of tracker point A, B and C is organised on the first, second and third row, respectively. The dashed red lines show the path of the tracked points. Also, the final deposition is represented by the dotted grey line and solid fuchsia line given by the PFEM and SPH-DEM, respectively. Some negligible differences can be appreciable in the velocity of the tracked points generated by both methods, as shown in Figure 18.

On the one hand, the results given by the coupled SPH-DEM are satisfactory despite its overestimation in the run-out distance and the deposit shape respect to the PFEM (Figure 18). This observation is caused by the overpredicted volumetric deformation that is typical in the SPH method that can happen even in static conditions as can be observed in [46].

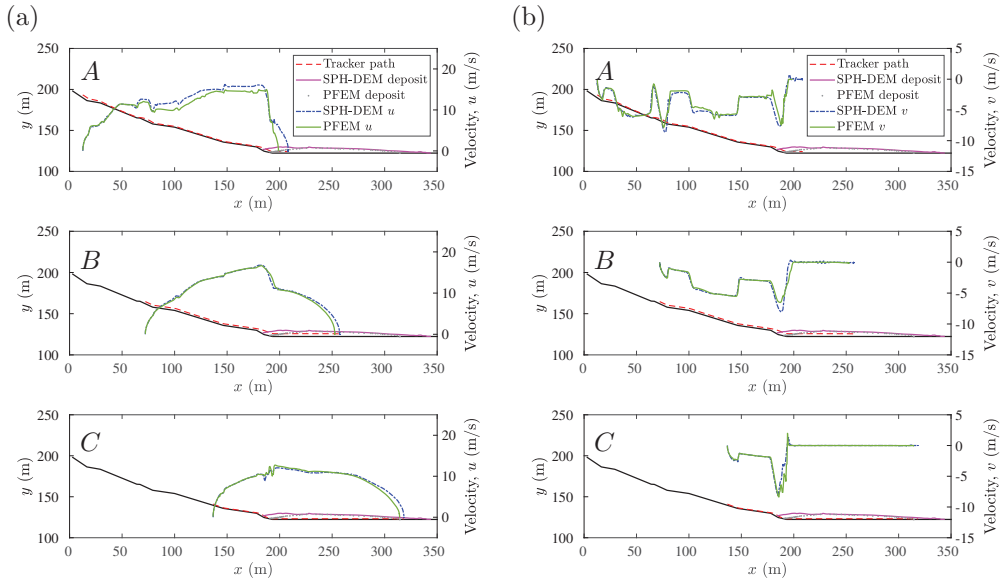

Figure 18: Comparison between SPH and PFEM. The solid green and dashed blue line are the velocity of the tracked point, A, B and C given by PFEM and SPH-DEM, respectively. The left and right–hand side column give the velocity in the x and y direction, respectively. The dashed red line represents the path of the tracked points. The solid black line represents the topography. The dotted grey and solid fuchsia lines are the final deposit shape obtained by PFEM and SPH-DEM, respectively.

6. Debris flow

After the validation of the SPH-DEM coupling either with fluid or soil by through four previous cases, the author desires to conclude this manuscript with a potential application of it for debris flow. Before any numerical description, it is crucial to define the limit of each phase to simulate the debris flow case.

The limits in the model will be established mainly based on sediment size, and it will be split into three "phases". First, as suggested by [10], particles with a silt-clay size can be taken as a part of the fluid since viscous forces dominate grain motion. Then, if the amount of such fine particles is enough to change the density and viscosity of the fluid phase, they must be considered in the Newtonian model. If the mineral composition and quantity of the fine particles are such that the viscosity becomes non-linear, then, another non-Newtonian constitutive model must be implemented for the fluid phase solely (e.g., exponential law or Herschel-Buckley, see [72]). Second, if the diameter is larger than silt size, as long as the grains keep in the frictional state, then another constitutive model might be implemented to describe the behaviour of the soil phase. Thus, an elastic perfectly-plastic constitutive model with Druker–Praguer failure criteria is employed in this work since it had demonstrated appropriated results in large deformation cases [23, 73, 26]. Third, it has been noticed that debris flows can drag big boulders which might have a diameter comparable to the flow depth and can reach 11 m in diameter [74, 10, 9]. The quantity and the size of such boulders in debris flows might be considered as singular values because the size is out of the characteristic diameters. Thus, large boulders are not included as part of the soil matrix that is represented through the continuum approach in this paper. Therefore, big boulders whose diameter is about the flow depth are represented as a "third phase" using DEM spheres.

Hence, a hypothetical example of debris flow is implemented to have a projection of its behaviour when all the materials (water, soil, and boulders) are combined at the same time. Thus, it is possible to test the coupling forces among all the materials in one single case, given by Equations 15, 19, 20, 25, 26. The configuration of this simulation is based on the case presented in section 5.4. However, several changes were performed in the initial configuration in such a way that it is not the intension of this section to reproduce the Yangbaodi landslide.

The topography is the same, plus two more DEM plates were added. A

horizontal one on the left–hand side to elongate the topography toward the back that will serve as an inflow condition of the water (Figure 19). Three boulders (DEM spheres) were placed into the fluid-soil mixture, as shown in Figure 19. The same shape of the initial profile in the dry case was employed but 3 m deeper in thickness, as shown in Figure 19. The soil was assumed to be 100 % saturated; so that the same shape of the initial condition for the soil was employed for water. The fluid and soil mass were discretised using a distance among points of $\Delta x = \Delta y = 0.5$ m, with a total of 7662 SPH points at the beginning and 8216 SPH particles at the end due to the inlet flow. The final time of the simulation was 30 s.

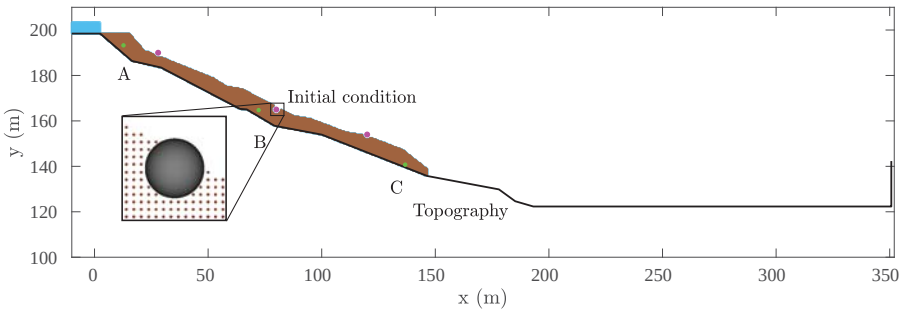

Figure 19: Initial configuration of the fluid and soil SPH particles, and DEM boulders (fuchsia points). Three soil SPH particles are tracked during the movement (green points A, B and C).

A Gumbel shaped function was employed to configure the velocity of the inlet flow during the half of the simulation, whereas the water level was kept constant, 5 m (see Equation 36 and Figure 20). Thus, it was possible to obtain a variable discharge upstream as might occur in dam-break or overtopping problems which are common in debris flows.

$$u = \frac{a_G}{\beta_G} \exp\left(-\frac{t-\mu_G}{\beta_G}\right) \exp\left[-\exp\left(-\frac{t-\mu_G}{\beta_G}\right)\right] \tag{36}$$

where $a_G = 35$, $\beta_G = 2$ and $\mu_G = 3$ are the parameter of the Gumbel function.

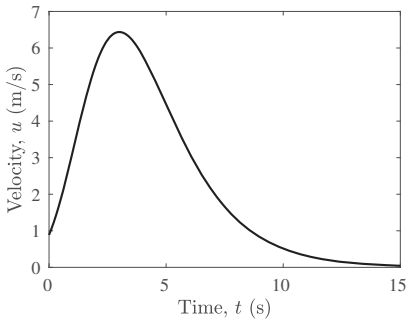

Figure 20: Hydrograph of the inlet flow.

Table 4: Debris flow parameters.

Parameter	Units	Value
Soil density, ρ_s	kg/m^3	2000
Friction angle, ϕ	$^\circ$	28
Dilation angle, ψ	$^\circ$	0
Young modulus, E	MPa	10
Cohesion, c	kPa	10
Intrinsic permeability, k_c	m^2	1×10^{-8}
Poisson ratio, ν		0.3
Porosity, n		0.428
Gravity, g	m/s^2	9.81
Boulder density, ρ_B	kg/m^3	2200
Boulder radius, R_B	m	2
Boulder friction coefficient, μ_ϕ		$\tan 18^\circ$
Bed friction coefficient, μ_ϕ		$\tan 18^\circ$
Fluid density, ρ_f	kg/m^3	2200
Fluid viscosity, μ	Pa·s	1×10^{-3}

Figure 21 shows the soil phase as well as the boulders descending by the slope at six time–steps. The colour map shows the magnitude of the velocity of each soil SPH particle. Figure 22 shows the fluid phase and the boulders

descending by the slope at the same six time–steps as in the soil phase. The colour map shows the magnitude of the velocity of each fluid SPH particle. It is possible to see form Figures 21 and 22 that the velocity in both phases are similar, and a slight difference can be noticed in the fluid phase mainly caused by the inlet flow. The fuchsia points denote the position of each boulder at that time step.

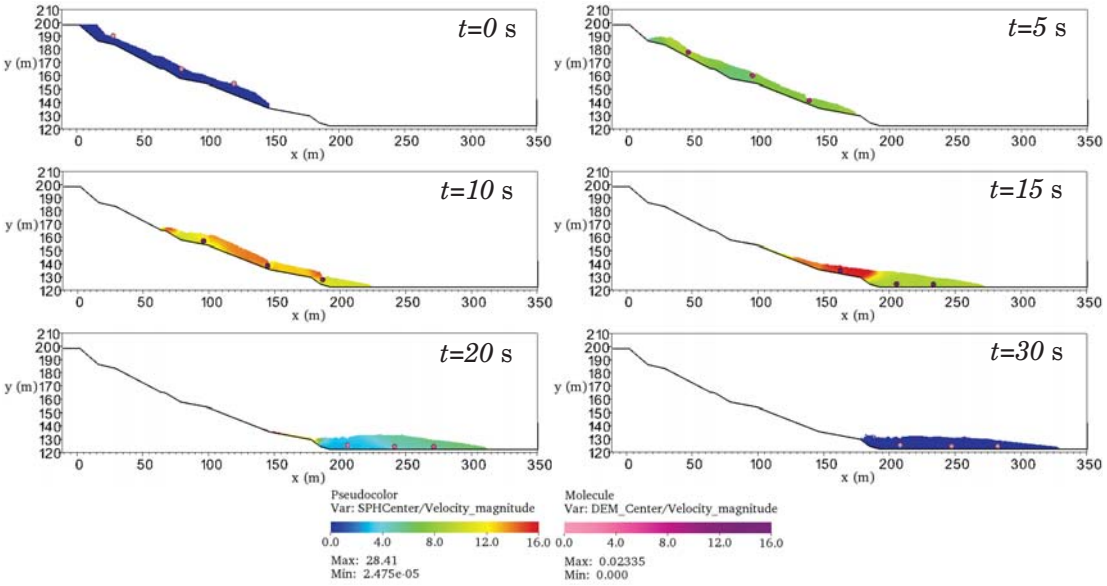

Figure 21: Norm of the velocity vector $|\mathbf{u}|$ of SPH soil particles and DEM boulders going down the slope.

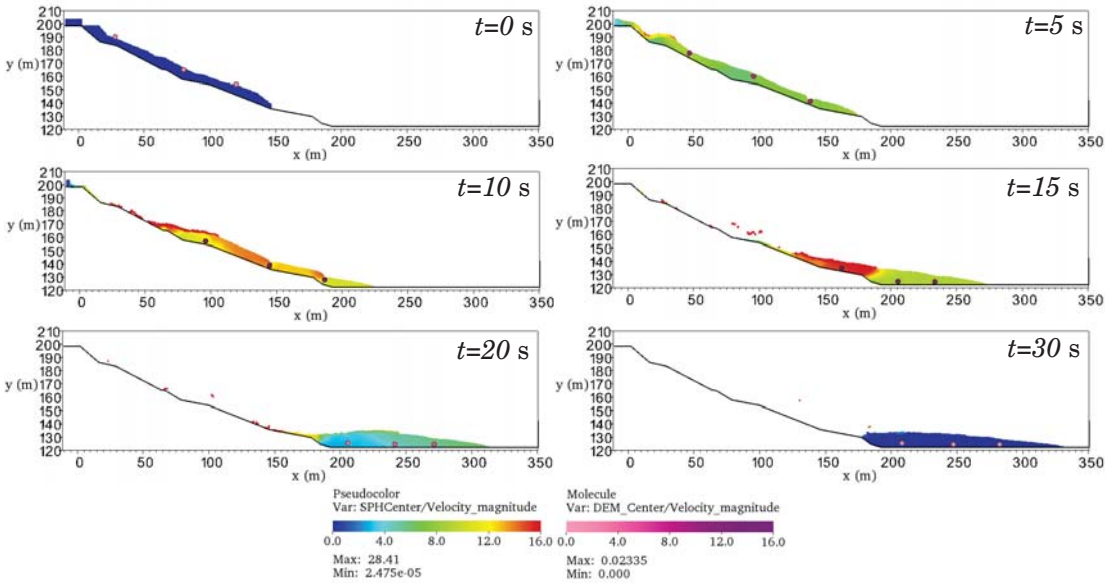

Figure 22: Norm of the velocity vector $|\mathbf{u}|$ of SPH soil particles and DEM boulders going down the slope.

Figures 23 and 24 present the colour map of the pore fluid pressure at the same six time steps. The most relevant characteristic is that the pore fluid pressure is interrupted horizontally by the presence of such big boulders. In contrast, the field of the pore fluid pressure seems to be more continuous in the x direction, in the absence of such boulders. Because of that, it is possible to see higher pore fluid pressure on the left side of the boulders and lower pressure on the right–hand side. It is noticeable specially at 10, 15 and 20 s (Figures 23 and 24).

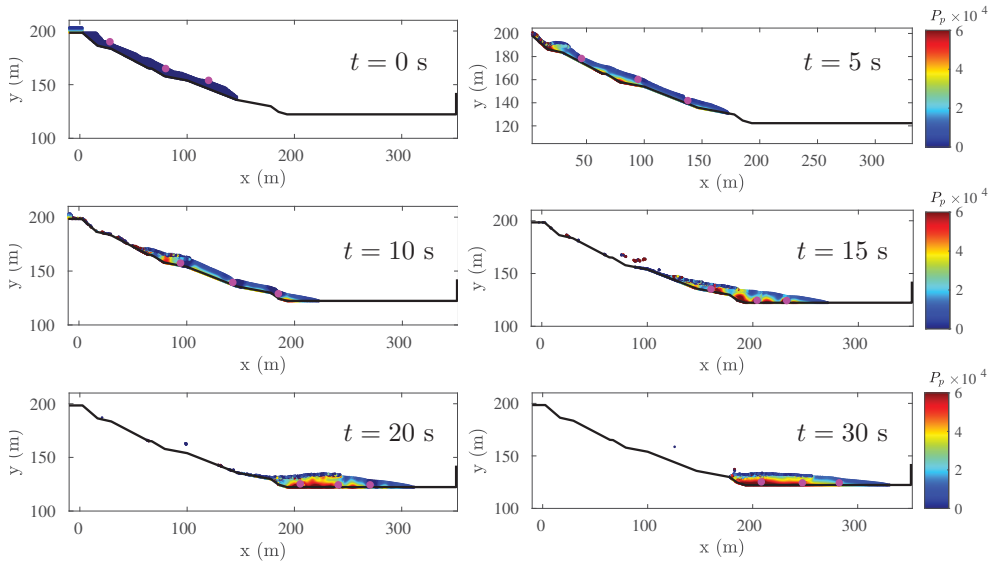

Figure 23: Pore fluid pressure during the displacement of the entire mass and boulders (fuchsia points).

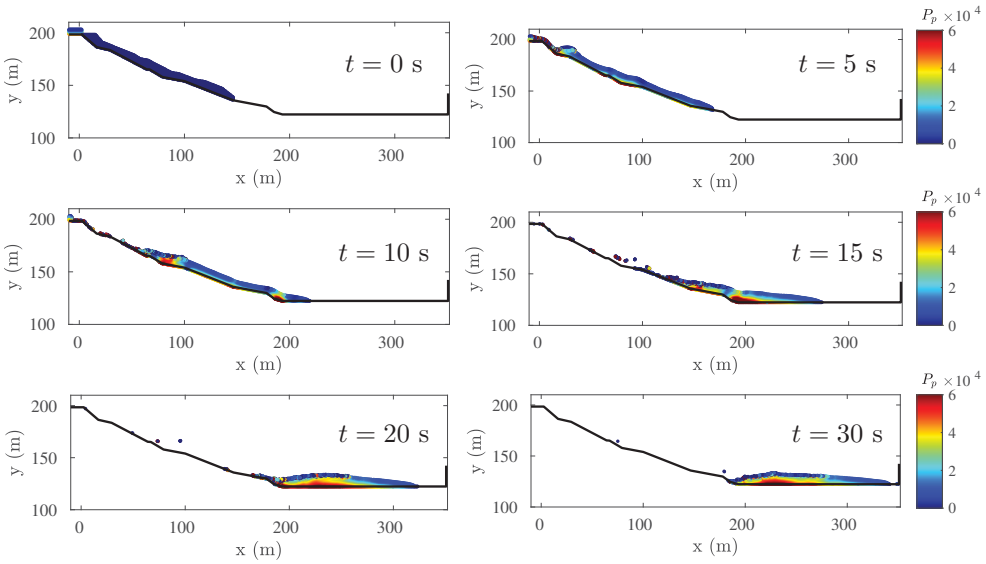

Figure 24: Pore fluid pressure during the displacement of the entire mass and boulders (fuchsia points).

Three trackers points were located precisely in the same position at the beginning of the simulation as in the dry landslide case 5.4. Figure 25 compares the velocity of the tracked points of the dry landslide to the debris flow with and without boulders. The velocity in x and y direction of the debris flow for each tracker point A, B and C is compared to the solution generated by the coupling SPH-DEM in the dry landslide in Figures 25a and 25b, respectively. The information of tracker points A, B and C is organised on by rows. The grey hatched area represents the final deposition of the entire fluid-soil mass, and the fuchsia points are the boulders. The solid orange line and dotted green line represent the velocity of the tracked point, A, B and C given by the debris flow, with and without boulders, respectively. The velocity that is given by the debris flow with boulders (solid orange line) and debris flow without boulders (dotted green line) has a very slight but still notable difference. The boulders seem to slow down and reduce the travel distance of the mass a few meters, unlike when the mixture does not have big boulders. This behaviour resembles

some descriptions given from observations in debris flow, where big boulders tend to retain materials on the rear part. Although this is not the proper case to study that characteristic due to the short travel distance, it starts to show a slow down process caused by the big boulders.

The aim of this section is not to reproduce the Yangbaodi landslide because of the abrupt changes given in the initial conditions. However, it is possible to observe in Figure 25 the similar velocities of the trackers points that were found changing the friction coefficient of the DEM segments on the topography from $\mu_\phi = \tan 10^\circ$ (dry case, Section 5.4) to $\mu_\phi = \tan 18^\circ$ (hypothetical debris flow). It shows the importance of the friction coefficient of this kind of events. Thus, the debris flow cases (solid orange line and dotted green line) show similar behaviour to the dry case (dashed blue line). This similarity is mainly due to the vertical restriction generated by the topography (see Figure 25b), whereas the velocity in x direction can be more affected by all the changes produced in the initial condition.

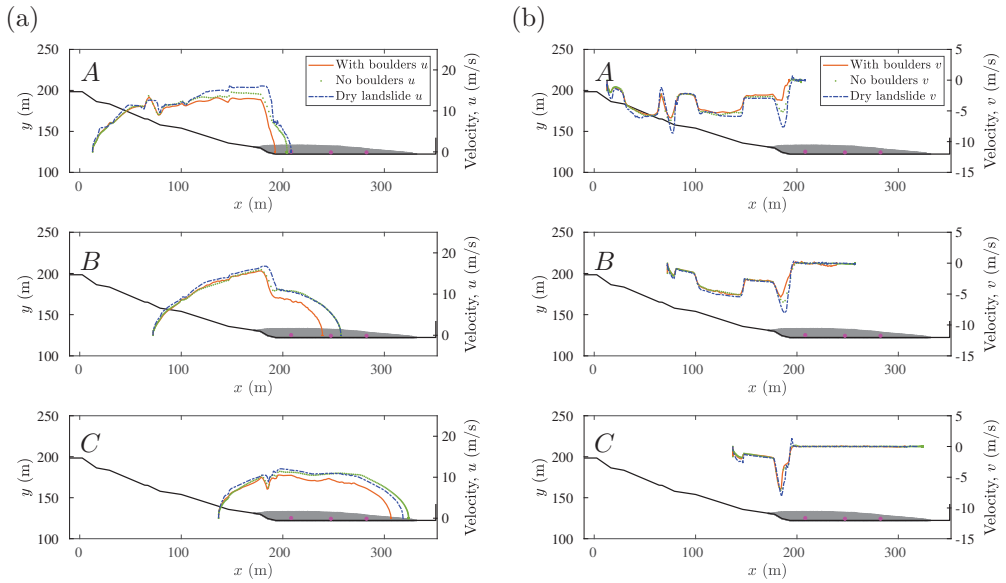

Figure 25: Comparison between dry landslide and debris flow with and without boulders. The solid orange line and dotted green line represent the velocity of the tracked point, A, B and C given by the debris flow, with and without boulders, respectively. The dashed blue line shows the velocity of the tracked point, A, B and C given by the dry landslide produced with SPH in Section 5.4. The left and right–hand side column give the velocity in the x and y direction, respectively. The grey hatched area is the profile of the final deposit of the fluid-soil mixture in addition to the boulders (fuchsia points).

On another hand, it is possible to obtain the information from the boulders such as their position, velocity and force exerted on them. Also, the potential E_P and kinetic energy E_K that the boulder possess by they self can be computed as follows,

$$E_P(t) = m_B g y_B = \rho_B \left(\frac{4}{3}\pi R_B^3\right) g y_B \tag{37}$$

$$E_K(t) = \frac{1}{2} m_B u_B^2 = \frac{1}{2}\rho_B \left(\frac{4}{3}\pi R_B^3\right) |\mathbf{u}|_B^2 \tag{38}$$

where m_B is the mass of the boulder and $|\mathbf{u}|_B$ is the magnitude of the velocity of the boulder. Figures 26a and 26b show the potential and kinetic

energy, respectively. From Figure 26a is evident that the boulders reach constant potential energy once they arrive in the flat area, whereas Figure 26b shows when the boulders lost all the kinetic energy at 23 s. Also, it is noticeable that the signal is noisy. However, it is caused by the dynamic of the process; the boulders have a variable velocity during the interaction with the other two phases, fluid and soil.

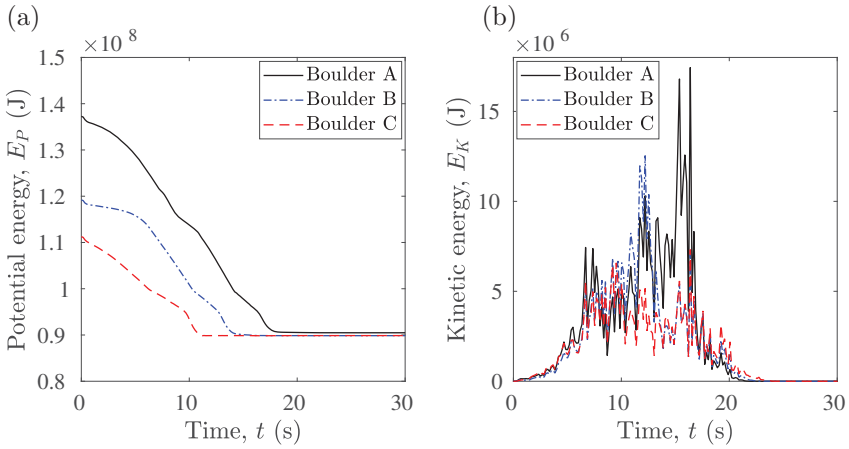

Figure 26: Energy versus time of each boulder during the flow. (a) potential energy. (b) kinetic energy.

Finally, the kinetic energy was checked from a control volume set up at the beginning of the horizontal zone (x=193.1 m) since this is the point were the mass reach the maximum velocity as can be verified in Figure 25. Any material (soil, fluid and boulders) that was crossing the control volume, whose width was $\Delta x = 0.5$ m, were added to obtain the total kinetic energy measured at that time (Figure 27). The equation that describe the total kinetic energy in the control volume at each time–step is given by,

$$E_{K(T)}(t) = \sum_{i}^{N} \frac{1}{2} m_i |\mathbf{u}|_i^2 + \frac{1}{2} m_B |\mathbf{u}|_B^2 \tag{39}$$

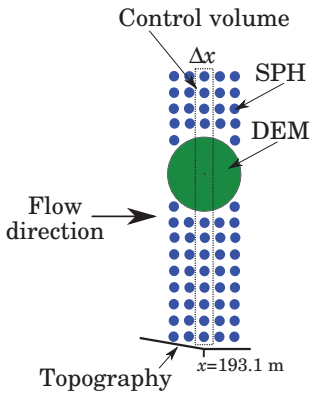

Figure 27: Scheme of the control volume to measure the kinetic energy as a function of time.

where N represents the total amount of SPH particles (soil and water) that are crossing the control volume at that specific time–step. The second term on the right–hand side will add the kinetic energy of a boulder as long as they are crossing the control volume. Figure 28 presents the kinetic energy of the numerical solution with boulders (solid black line) and without boulders (dashed blue line) into the mixture. The simulation with no boulders is employed as a reference case to observe the importance of including big and heavy objects into the simulations when required. Figure 28 shows that the average behaviour which is given by the SPH particles in both cases is similar.

Also, it is noticeable when each boulder is crossing the control volume since the kinetic energy increases five times, which is marked by the three peaks in Figure 28. The boulders are decreasing the dissipation rate of the kinetic energy while they are moving, which increases the potential of damage. Such an increment is not just given by the mass of the boulder taken into account in the control volume, but by their velocities; as one is zero, there is not kinetic energy coming from DEM spheres. [75] have demonstrated that the force coefficient, which is employed to estimate the impact force on rigid barriers, is strongly dependent on both the diameter of the particles and the Froude number of the flow. Larger particles have a higher force coefficient, increasing the impact force. The quantitative estimation of the energy and force in such kind of phenomena

is essential to consider the damage level of a specific structure or to provide data for designing of the retention structures.

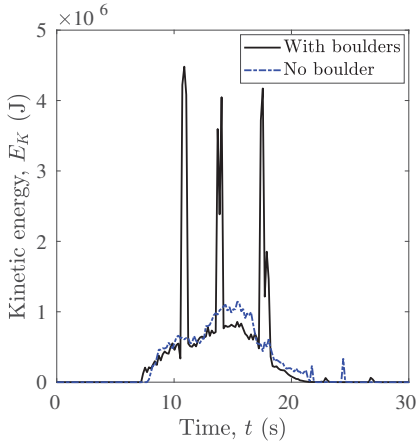

Figure 28: Measurement if the kinetic energy at the distance of $x = 193.1$ m for the entire depth of the flow with boulders (black line) and with no boulders (blue line).

The results presented in this section, especially where it is shown the difference in the behaviour of debris flow with and without boulders (Figures 23, 24, 25 and 27), highlight the importance of including all the materials (fluid, soil and big boulders) to have a better understanding of dynamic of debris flow. The SPH-DEM coupled method provides a promising tool that will help to study the interaction of big boulders with the rest of the debris flow mixture, which is still poorly understood as pointed out by [9]. Additionally, it might be possible to get more accurate data no just to design retention structures but to compute the potentially affected areas. Despite the promising benefits, validation for such type of phenomena is still required.

7. Conclusions

The coupling SPH–DEM produces satisfactory results in all the benchmark cases here implemented, which is verified by analytical solutions, experimental

measurements and field data. Also, the force exerted on the DEM elements is obtained straightforwardly; no extra computations are needed.

The main advantage of the coupling methodology here implemented relies on two facts. There is no longer concern that particles can penetrate the wall, as can occur with traditional treatments on the boundary conditions for SPH solvers. This method avoids the penetration of the moving SPH particles entirely through the boundary conditions. Moreover, the computational effort produced to calculate the variables such as velocity, pressure and stresses for particles that belong to the boundary conditions is wholly avoided.

The coupled method can predict the force for both stationary and transient cases since the results match with reasonable accuracy the analytical solutions and experimental data. The tangential force is the one that has a dominant role in differentiating if a DEM object is interacting with fluid or soil SPH particles. In contrast, the normal force is treated indistinct of the interacting material.

The velocity profile produced in the Poiseuille flow is quite the same if SPH or DEM boundary conditions are implemented. Also, the force had a low order of error $O(10^{-6})$ regards the analytical solution here presented. Appropriate results were also found in the case of a square array of cylinders to obtain the permeability and drag force.

The impact force presented in the experimental dry granular flow is acceptable despite the overestimation. It was also found that the friction angle, the basal friction coefficient and artificial viscosity coefficients make a significant contribution to the impact force. Furthermore, the dry large scale landslide simulation showed similar behaviour regards other numerical techniques. The established tangential force term generates appropriate results as demonstrated mainly through the velocity of the mass as noticeable in the dry landslide case.

The projection of this numerical strategy toward debris flows shows consistent results: velocity, deposit profile and energy show realistic behaviour. A significant difference could be noticed when big boulders are crossing the control volume as well as the soil and fluid materials, which can contribute to structure design of retaining dams for debris flows.

Some differences in pore fluid pressure field and velocity were found when the big boulders are introduced in debris flows, in regards to their absence. However, the coupled SPH–DEM still requires validation for such kind of phenomena.

Acknowledgements

The authors acknowledge the financial support from Westlake University and access to the Westlake University Supercomputer Center. The first author was supported by the scholarship from CeiBA Foundation to study his doctorate. The first author would like to express his thankfulness to Dr Maziar Gholami Korzani for the helpful discussions on the SPH code.

References

[1] R. L. Schuster, R. W. Fleming, Economic losses and fatalities due to landslides, Bulletin of the Association of Engineering Geologists 23 (1) (1986) 11–28.

[2] N. Hilker, A. Badoux, C. Hegg, The swiss flood and landslide damage database 1972-2007, Natural Hazards and Earth System Sciences 9 (3) (2009) 913.

[3] O. Kjekstad, L. Highland, Economic and social impacts of landslides, in: Landslides–disaster risk reduction, Springer, 2009, pp. 573–587.

[4] D. J. Varnes, Slope movement types and processes, Special report 176 (1978) 11–33.

[5] T. C. Pierson, J. E. Costa, A rheologic classification of subaerial sediment-water flows, Debris flows/avalanches: process, recognition, and mitigation. Reviews in Engineering Geology 7 (94) (1987) 1–12.

[6] P. Coussot, M. Meunier, Recognition, classification and mechanical description of debris flows, Earth-Science Reviews 40 (3) (1996) 209–227.

[7] O. Hungr, S. Evans, M. Bovis, J. Hutchinson, A review of the classification of landslides of the flow type, Environmental & Engineering Geoscience 7 (3) (2001) 221–238.

[8] M. Jakob, A size classification for debris flows, Engineering geology 79 (3) (2005) 151–161. doi:doi:10.1016/j.enggeo.2005.01.006.

[9] T. Takahashi, Debris flow: mechanics, prediction and countermeasures, CRC press, 2014.

[10] R. M. Iverson, The physics of debris flows, Reviews of Geophysics 35 (3) (1997) 245–296. doi:Papernumber97RG00426.

[11] S. B. Savage, K. Hutter, The motion of a finite mass of granular material down a rough incline, Journal of Fluid Mechanics 199 (1989) 177–215. doi:10.1017/S0022112089000340.

[12] R. P. Denlinger, R. M. Iverson, Granular avalanches across irregular three-dimensional terrain: 1. theory and computation, Journal of Geophysical Research 109 (F1). doi:doi:10.1029/2003JF000085.

[13] Y. Wang, K. Hutter, S. P. Pudasaini, The savage-hutter theory: A system of partial differential equations for avalanche flows of snow, debris, and mud, ZAMM-Journal of Applied Mathematics and Mechanics/Zeitschrift für Angewandte Mathematik und Mechanik: Applied Mathematics and Mechanics 84 (8) (2004) 507–527.

[14] M. Christen, J. Kowalski, P. Bartelt, Ramms: Numerical simulation of dense snow avalanches in three-dimensional terrain, Cold Regions Science and Technology 63 (1) (2010) 1–14.

[15] R. M. Iverson, R. P. Denlinger, Flow of variably fluidized granular masses across three-dimensional terrain: 1. coulomb mixture theory, Geophysical Research Journal 106 (B1) (2001) 537–552. doi:Papernumber2000JB900329.

[16] S. P. Pudasaini, Y. Wang, K. Hutter, Modelling debris flows down general channels, Natural Hazards and Earth System Science 5 (0) (2005) 799–819. doi:SRef-ID:1684-9981/nhess/2005-5-799.

[17] T. Takahashi, H. Nakagawa, Flood/debris flow hydrograph due to collapse of a natural dam by overtopping, Journal of hydroscience and Hydraulic Engineering 12 (2) (1994) 41–49.

[18] E. B. Pitman, L. Le, A two-fluid model for avalanche and debris flows, Philosophical Transactions of the Royal Society of London A: Mathematical, Physical and Engineering Sciences 363 (1832) (2005) 1573–1601.

[19] S. P. Pudasaini, A general two-phase debris flow model, Journal of Geophysical Research: Earth Surface 117 (F3) (2012) 799–819.

[20] G. Córdoba, G. Villarosa, M. Sheridan, J. Viramonte, D. Beigt, G. Salmuni, Secondary lahar hazard assessment for villa la angostura, argentina, using two-phase-titan modelling code during 2011 cordón caulle eruption, Natural Hazards and Earth System Sciences 15 (4) (2015) 757–766. doi:doi:10.5194/nhess-15-757-2015.

[21] Z. Dai, Y. Huang, H. Cheng, Q. Xu, Sph model for fluid–structure interaction and its application to debris flow impact estimation, Landslides 14 (3) (2017) 917–928.

[22] J. J. Monaghan, Smoothed particle hydrodynamics, Reports on progress in physics 68 (8) (2005) 1703–1759.

[23] H. H. Bui, R. Fukagawa, K. Sako, S. Ohno, Lagrangian meshfree particles method (sph) for large deformation and failure flows of geomaterial using elastic–plastic soil constitutive model, International Journal for Numerical and Analytical Methods in Geomechanics 32 (12) (2008) 1537–1570.

[24] C. Peng, X. Guo, W. Wu, Y. Wang, Unified modelling of granular media with smoothed particle hydrodynamics, Acta Geotechnica 11 (6) (2016) 1231–1247.

[25] A. M. Abdelrazek, I. Kimura, Y. Shimizu, Simulation of three-dimensional rapid free-surface granular flow past different types of obstructions using the sph method, Journal of Glaciology 62 (232) (2016) 335–347.

[26] C. T. Nguyen, C. T. Nguyen, H. H. Bui, G. D. Nguyen, R. Fukagawa, A new sph-based approach to simulation of granular flows using viscous damping and stress regularisation, Landslides 14 (1) (2017) 69–81.

[27] M. G. Korzani, S. Galindo-Torres, A. Scheuermann, D. Williams, Smoothed particle hydrodynamics for investigating hydraulic and mechanical behaviour of an embankment under action of flooding and overburden loads, Computers and Geotechnics 94 (2018) 31–45.

[28] M. G. Korzani, S. Galindo-Torres, A. Scheuermann, D. Williams, Sph approach for simulating hydro-mechanical processes with large deformations and variable permeabilities, Acta Geotechnica 13 (2) (2018) 303–316.

[29] A. V. Potapov, M. L. Hunt, C. S. Campbell, Liquid–solid flows using smoothed particle hydrodynamics and the discrete element method, Powder Technology 116 (2-3) (2001) 204–213.

[30] Y. Cui, A. Nouri, D. Chan, E. Rahmati, A new approach to dem simulation of sand production, Journal of Petroleum Science and Engineering 147 (2016) 56–67.

[31] B. Nassauer, T. Liedke, M. Kuna, Development of a coupled discrete element (dem)–smoothed particle hydrodynamics (sph) simulation method for polyhedral particles, Computational Particle Mechanics 3 (1) (2016) 95–106.

[32] J. Wang, D. Chan, Frictional contact algorithms in sph for the simulation of soil–structure interaction, International Journal for Numerical and Analytical Methods in Geomechanics 38 (7) (2014) 747–770.

[33] P. A. Cundall, O. D. Strack, A discrete numerical model for granular assemblies, Geotechnique 29 (1) (1979) 47–65.

[34] S. Galindo-Torres, A coupled discrete element lattice boltzmann method for the simulation of fluid–solid interaction with particles of general shapes, Computer Methods in Applied Mechanics and Engineering 265 (2013) 107–119.

[35] H. Tan, S. Chen, A hybrid dem-sph model for deformable landslide and its generated surge waves, Advances in Water Resources 108 (2017) 256–276.

[36] W.-J. Xu, Z.-G. Yao, Y.-T. Luo, X.-Y. Dong, Study on landslide-induced wave disasters using a 3D coupled SPH-DEM method, Bulletin of Engineering Geology and the Environment 79 (1) (2020) 467–483. doi:10.1007/s10064-019-01558-3.

[37] A. Leonardi, F. K. Wittel, M. Mendoza, R. Vetter, H. J. Herrmann, Particlefluidstructure interaction for debris flowimpact on flexible barriers, Computer-Aided Civil and Infrastructure Engineering 31 (2016) 323–333.

[38] C. Liu, Q. Sun, G. G. D. Zhou, Coupling of material point method and discrete element method for granular flows impacting simulations, International Journal for Numerical Methods in Engineering 115 (2) (2018) 172–188. doi:10.1002/nme.5800.

[39] X. Li, J. Zhao, A unified cfd-dem approach for modeling of debris flow impacts on flexible barriers: A unified cfd-dem approach for modeling of debris flow impacts on flexible barriers, International Journal for Numerical and Analytical Methods in Geomechanics 42 (14) (2018) 1643–1670. doi:10.1002/nag.2806.

[40] J. L. González Acosta, P. J. Vardon, G. Remmerswaal, M. A. Hicks, An investigation of stress inaccuracies and proposed solution in the material point method, Computational Mechanics 65 (2019) 555–581.

[41] S. Galindo-Torres, D. Pedroso, Molecular dynamics simulations of complex-shaped particles using voronoi-based spheropolyhedra, Physical Review E 81 (6) (2010) 061303.

[42] R. A. Gingold, J. J. Monaghan, Smoothed particle hydrodynamics: theory and application to non-spherical stars, Monthly notices of the royal astronomical society 181 (3) (1977) 375–389.

[43] L. B. Lucy, A numerical approach to the testing of the fission hypothesis, The astronomical journal 82 (1977) 1013–1024.

[44] J. J. Monaghan, An introduction to sph, Computer physics communications 48 (6) (2009) 861–872.

[45] M. Liu, G. Liu, Smoothed particle hydrodynamics (sph): an overview and recent developments, Archives of computational methods in engineering 17 (1) (2010) 25–76.

[46] M. Antuono, A. Colagrossi, S. Marrone, Numerical diffusive terms in weakly-compressible sph schemes, Computer Physics Communications 183 (12) (2012) 2570–2580.

[47] D. Molteni, A. Colagrossi, A simple procedure to improve the pressure evaluation in hydrodynamic context using the sph, Computer Physics Communications 180 (6) (2009) 861–872.

[48] J. P. Morris, P. J. Fox, Y. Zhu, Modeling low reynolds number incompressible flows using sph, Journal of computational physic 136 (1) (1997) 214–226.

[49] P. W. Cleary, J. J. Monaghan, Conduction modelling using smoothed particle hydrodynamics, Journal of Computational Physics 148 (1) (1999) 227–264.

[50] J. P. Morris, Simulating surface tension with smoothed particle hydrodynamics, International journal for numerical methods in fluids 33 (3) (2000) 333–353.

[51] M. G. Korzani, S. A. Galindo-Torres, A. Scheuermann, D. J. Williams, Parametric study on smoothed particle hydrodynamics for accurate de-

termination of drag coefficient for a circular cylinder, Water Science and Engineering 10 (2) (2017) 143–153.

[52] J. J. Monaghan, Sph without a tensile instability, Journal of Computational Physics 159 (2) (2000) 290–311.

[53] H. H. Bui, K. Sako, R. Fukagawa, Numerical simulation of soil–water interaction using smoothed particle hydrodynamics sph method, Journal of Terramechanics 44 (5) (2007) 339–346. doi:10.1016/j.jterra.2007.10.003.

[54] H. H. Bui, G. D. Nguyen, A coupled fluid-solid sph approach to modelling flow through deformable porous media, International Journal of Solids and Structures 125 (2017) 244–264.

[55] M. B. Kirkham, Principles of soil and plant water relations, 2nd Edition, Academic Press, 2014.

[56] M. R. Islam, K. Hayano, M. A. Rahman, Insights into effects of seepage on failure of breakwater mound: Experimental and numerical investigations, Indian Geotechnical Journal 49 (5) (2019) 531–542.

[57] M. R. Islam, M. A. Rahman, K. Hayano, Application of smoothed particle hydrodynamics (sph) for simulating various geotechnical problems, SN Applied Sciences 2 (4) (2020) 1–14.

[58] S. Galindo-Torres, D. Pedroso, D. Williams, L. Li, Breaking processes in three-dimensional bonded granular materials with general shapes, Computer Physics Communications 183 (2) (2012) 266–277.

[59] M. Otsubo, C. O'Sullivan, T. Shire, Empirical assessment of the critical time increment in explicit particulate discrete element method simulations, Computers and Geotechnics 86 (2017) 67–79.

[60] J. Wang, H. Wu, C. Gu, H. Hua, Simulating frictional contact in smoothed particle hydrodynamics, Science China Technological Sciences 56 (7) (2013) 1779–1789.

[61] J. Wang, H. Hua, C. Gu, On the correction of the boundary deficiency in sph for the frictional contact simulation, Science China Technological Sciences 57 (1) (2014) 86–100.

[62] Y. Wang, S. Abe, S. Latham, P. Mora, Implementation of particle-scale rotation in the 3–d lattice solid model, in: Computational Earthquake Physics: Simulations, Analysis and Infrastructure, Part I, Springer, 2006, pp. 1769–1785.

[63] S. Galindo-Torres, F. Alonso-Marroquín, Y. Wang, D. Pedroso, J. M. Castano, Molecular dynamics simulation of complex particles in three dimensions and the study of friction due to nonconvexity, Physical Review E 79 (6) (2009) 060301.

[64] P. Adler, Porous media: geometry and transports, Elsevier, 2013.

[65] A. S. Sangani, A. Acrivos, Slow flow past periodic arrays of cylinders with application to heat transfer, International journal of Multiphase flow 8 (3) (1982) 193–206.

[66] S. Moriguchi, R. I. Borja, A. Yashima, K. Sawada, Estimating the impact force generated by granular flow on a rigid obstruction, Acta Geotechnica 4 (1) (2009) 57–71.

[67] H. Teufelsbauer, Y. Wang, S. P. Pudasaini, R. Borja, W. Wu, Dem simulation of impact force exerted by granular flow on rigid structures, Acta Geotechnica 6 (3) (2011) 119–133. doi:DOI10.1007/s11440-011-0140-9.

[68] X. He, D. Liang, W. Wu, G. Cai, C. Zhao, S. Wang, Study of the interaction between dry granular flows and rigid barriers with an sph model, International Journal for Numerical and Analytical Methods in Geomechanics 42 (11) (2018) 1217–1234.

[69] S. Adami, X. Y. Hu, N. A. Adams, A generalized wall boundary condition for smoothed particle hydrodynamics, Journal of Computational Physics 231 (21) (2016) 7057–7075.

[70] X. Zhang, K. Krabbenhoft, D. Sheng, W. Li, Numerical simulation of a flow-like landslide using the particle finite element method, Computational Mechanics 55 (1) (2015) 167–177.

[71] W. C. Li, H. J. Li, F. Dai, L. M. Lee, Discrete element modeling of a rainfall-induced flowslide, Engineering geology 149 (2012) 22–34.

[72] G. d. F. Maciel, H. K. d. Santos, F. d. O. Ferreira, Rheological analysis of water clay compositions in order to investigate mudflows developing in canals, Journal of the Brazilian Society of Mechanical Sciences and Engineering 31 (1) (2009) 64–74.

[73] W. Chen, T. Qiu, Numerical simulations for large deformation of granular materials using smoothed particle hydrodynamics method, International Journal of Geomechanics 12 (2) (2012) 127–135.

[74] M. Larsen, G. Wieczorek, L. Eaton, B. Morgan, H. Torres-Sierra, Natural hazards on alluvial fans; the venezuela debris flow and flash flood disaster, Tech. Rep. 103-01, USGS (2002).

[75] Y. Cui, C. E. Choi, L. H. Liu, C. W. Ng, Effects of particle size of monodisperse granular flows impacting a rigid barrier, Natural Hazards 91 (3) (2018) 1179–1201.